JOURNAL OF COMPUTATIONAL PHYSICS **125,** 161–176 (1996)
ARTICLE NO. 0086

A Model for Laser Hole Drilling in Metals

RAM K. GANESH,* WALLACE W. BOWLEY,* ROBERT R. BELLANTONE,† AND YUKAP HAHN†

*Department of Mechanical Engineering, University of Connecticut, Storrs, Connecticut 06269-3139; †Department of Physics, University of Connecticut, Storrs, Connecticut 06269-3046

Received December 2, 1994; revised October 5, 1995

A direct computer simulation technique is developed to analyze quantitatively the influence of the fluid flow and heat transfer in the transient development of a laser drilled hole in a turbine airfoil material, where the material removal is effected by vaporization and melt ejection. The coupled conduction heat transfer in the solid and the advection-diffusion heat transfer in the liquid metal, the fluid dynamics of melt expulsion and the tracking of solid–liquid and liquid–vapor interfaces have been mathematically modeled for the 2D axisymmetric case. The donor–acceptor cell method using the volume of fluid approach is used to solve the complex problem and a versatile numerical code has been developed. It takes into account all thermophysical properties including latent heat of vaporization, gravity, and surface tension driving forces. The novelty of this model is to treat the melted pool surface as a deformable free surface. The impressed pressure and temperature on the melt surface is provided by an 1D gas dynamics model whose vaporization kinetics are also discussed. The model is used to simulate drilling for a number of spatially and temporally varying laser intensity profiles. It is found that resolidification of melt (recast formation) occurred throughout the pulse interval and had significant effect on the developing hole geometry, while the effect of vaporization material removal on the hole geometry is found to be small. Comparison of the simulated results indicates the material removed per joule of energy absorbed appears to be inversely proportional to the square root of the peak beam intensity and the drilling rate appears to be proportional to the square root of the surface pressure.

1. INTRODUCTION

The process of laser drilling of aircraft turbine blades needs to be clearly understood from a fundamental standpoint both to control, as well as to increase, the efficiency of the process. The minute holes of the order of 0.020 in in diameter drilled in a batch process do not possess the same geometry or size (many times neither one), resulting in the unsuitability of the component or operational hazards in the actual service environment. Lasers have become an accepted tool in the drilling of these holes but still need a trial and error procedure. In the LD (laser drilling) process, it becomes next to impossible to measure routinely the temperatures, the pressure and the flow conditions in the laser melted pool due to the size of the pool, the extreme nature of the temperatures and pressures generated, inaccessibility due to the size of the hole, and last but not least, the presence of the laser beam itself. Typical temperature gradients encountered are of the order of 10^{6o} K/cm. Power density of 0.1 to 20 MW/cm^2 is typically used in laser drilling wherein momentum transport or convection is significant. Vaporization and gas dynamical effects become predominant too. Numerical modeling helps understand the competing complex phenomena that occur simultaneously during drilling, either individually or in concert and lets one gauge their relative importance as well.

A schematic representation of the LD process is shown in Fig. 1. A laser beam is produced and directed toward a metal target, which absorbs some fraction of the incident light energy. Vaporization that occurs after melting creates a back (recoil) pressure on the melt surface which pushes the melt away in the radial direction. Thus, the material is removed by a combination of vaporization and liquid expulsion. The physical processes that take place during material removal are heat transfer into the metal, thermodynamics of phase-changes, and incompressible fluid flow due to the impressed pressure, with a free boundary at the melt/vapor interface and a moving boundary at the melt/solid interface. The presence of melting and solidification in the modeling of LD process makes it a moving boundary (or moving interface) problem. The liquid and solid phases of different thermophysical properties are separated by the moving melt–solid interface and at which thermal energy is either absorbed or liberated. The other, also moving, liquid–vapor boundary is a free boundary. This kind of problem is termed *Stefan* problem with two moving boundaries, where *Stefan* boundary conditions are enforced.

The effects of fluid flow and convection on the melted pools in welding were reported as early as the 1950s and an overview of the melt dynamics is provided by Mazumder [1]. A summary of theoretical work on weld pool fluid flow and heat transfer is given by Zacharia *et al.* [2]. Two-dimensional transient model for surface tension driven pool was developed by Chan *et al* [3]. The model is formulated in such a way that the solid–liquid interface is obtained as part of the solution. The surface of the melt pool is assumed to be flat to facilitate application of the boundary conditions. Temperature flux boundary condi-

0021-9991/96 $18.00

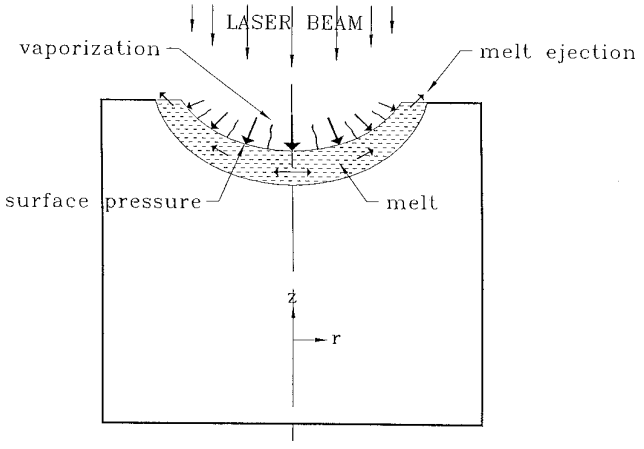

FIG. 1. Schematic diagram of laser drilling process. The laser beam causes melting and then vaporization creating a back pressure on the liquid surface which pushes the melt away.

tion is applied at the top surface. A three-dimensional quasi-steady state model for convection in laser melted pool is developed by Kou and Wang [4] which takes into account surface tension and buoyancy driving forces. A Gaussian temperature flux boundary condition is applied at the top surface which is again assumed flat. A conjugate heat transfer method [5] using enthalpy-temperature and viscosity-temperature relationships is employed to obtain solid–liquid interface as part of the solution. Curently researchers are working on three-dimensional models for laser melted pools. A three-dimensional transient model for arc welding process by Zacharia *et al.* [2] is formulated to obtain the solid–liquid interface as a part of the solution and treats the pool surface as a free, open surface that can undergo temporal and spatial variations.

In the laser–metal interactions investigations Chan and Mazumder [6] have devised a one-dimensional steady-state model which furnishes closed form analytical solutions for damage by liquid expulsion and vaporization. Another one-dimensional theoretical model for rate of vaporization and liquid expulsion was used by Von Allman [7] to calculate the velocity and the efficiency of laser drilling as a function of the absorbed intensity. A two-dimensional model for damage due to melting and vaporization formulated by Kar and Mazumder [8], is based on the energy conservation equation and the effects of various parameters on the depth and the radius of holes drilled are studied numerically. A theoretical gas-assisted laser–metal drilling model is developed by Patel and Brewster [9] for low-power laser–metal interaction and does not apply to situations where incident laser fluxes are high enough to produce significant vaporization at the metal surface.

The time dependent solution obtained in the 2D axisymmetric case in the present model predicts the transient development of the drilled hole, as well as the expulsion of the liquid metal, and contains, as part of the solution, the solid–liquid and the liquid–vapor interface positions (the solution is said to be self-consistent). The novel features of this model are:

1. The top surface of the laser melted pool is treated as a free surface and spatially and temporally varying temperature and pressure boundary conditions are applied on it. A gas dynamics model whose vaporization kinetics are discussed in Section 2.1.2 furnishes the temperature and pressure boundary conditions as a function of the absorbed laser intensity.
2. The resolidification of the molten metal when the thermal energy is discontinued or inadequate to sustain melt is taken into account.

Molten metal flow can influence the temperature gradient at the solid–liquid interface and the cooling rate through certain critical temperature ranges, thereby influencing the recast formation, pool shape, aspect ratio, and ripples at the free deformable surface. The code SOLA-VOF [10] is extensively modified for LD simulation and its modular fashion is conducive to singling out an effect (e.g., surface tension, gravity) and studying the combined effect of the rest of the complex phenomena, enabling us to get a feel for the absence of that individual effect on the laser drilling process.

2. THEORETICAL DEVELOPMENT

The specific theoretical bases adopted for the LD model are summarized in this section, most of which are well known. Several key approximations and assumptions introduced are explicitly stated.

2.1. Field Equations

2.1.1. *Fluid Flow and Heat Transfer*

The field equations are the conservation of mass, the Navier–Stokes equations (the conservation of linear momentum), and the thermal energy equation in cylindrical coordinates,

$$\frac{\partial u}{\partial r} + \frac{\partial v}{\partial z} + \frac{u}{r} = 0, \qquad [2.1.1.1]$$

$$\frac{\partial u}{\partial t} + u\frac{\partial u}{\partial r} + v\frac{\partial u}{\partial z} = \frac{\mu}{\rho}\left[\frac{\partial^2 u}{\partial r^2} + \frac{\partial^2 u}{\partial z^2} + \frac{1}{r}\frac{\partial u}{\partial r} - \frac{u}{r^2}\right] - \frac{1}{\rho}\frac{\partial p}{\partial r}, \qquad [2.1.1.2]$$

$$\frac{\partial v}{\partial t} + u\frac{\partial v}{\partial r} + v\frac{\partial v}{\partial z} = \frac{\mu}{\rho}\left[\frac{\partial^2 v}{\partial r^2} + \frac{\partial^2 v}{\partial z^2} + \frac{1}{r}\frac{\partial v}{\partial r}\right] - \frac{1}{\rho}\frac{\partial p}{\partial z} - g,$$

$$\frac{\partial T}{\partial t} + u\frac{\partial T}{\partial r} + v\frac{\partial T}{\partial z} = \alpha\left[\frac{\partial^2 T}{\partial r^2} + \frac{\partial^2 T}{\partial z^2} + \frac{1}{r}\frac{\partial T}{\partial r}\right]. \quad [2.1.1.3]$$

The non-dimensionalized variables are defined as

$$u^* = \frac{u}{u_0},$$

$$v^* = \frac{v}{u_0}, \quad [2.1.1.4]$$

$$g^* = \frac{g d_0}{u_0^2} = \frac{1}{\mathrm{Fr}^2},$$

$$\sigma^* = \frac{\gamma_{st}}{\rho u_0^2 d_0} = \frac{1}{\mathrm{We}},$$

$$p^* = \frac{p}{\rho u_0^2},$$

$$r^* = \frac{r}{d_0},$$

$$y^* = \frac{y}{d_0},$$

$$T^* = \frac{T - T_0}{T_{\mathrm{Ref}} - T_0},$$

$$\mathrm{Re} = \frac{\rho u_0 d_0}{\mu},$$

$$\mathrm{Pe} = \frac{u_0 d_0}{\alpha},$$

$$t^* = \frac{t u_0}{d_0},$$

$$= F_0 Pe,$$

$$F_0 = \frac{\alpha t}{d_0^2},$$

The characteristic length, d_0, and the characteristic velocity, u_0, are taken as 508 μm which is the diameter of a typical laser beam and 10 cm/s, respectively. The various non-dimensionalized numbers are as follows: Re, the ratio of inertia forces to viscous forces; Pe, the ratio of rate of heat convection to rate of heat conduction; F_0, a dimensionless time in the thermal conduction equation or the ratio of rate of heat conduction to rate of thermal energy storage in a solid; Fr, the ratio of inertia forces to gravity forces; and We characterizes the surface tension effect. The above equations result (dropping the asterisks) in the set of non-dimensional equations,

$$\frac{\partial u}{\partial r} + \frac{\partial v}{\partial z} + \frac{u}{r} = 0, \quad [2.1.1.5]$$

$$\frac{\partial u}{\partial t} + u\frac{\partial u}{\partial r} + v\frac{\partial u}{\partial z} = \frac{1}{\mathrm{Re}}\left[\frac{\partial^2 u}{\partial r^2} + \frac{\partial^2 u}{\partial z^2} + \frac{1}{r}\frac{\partial u}{\partial r} - \frac{u}{r^2}\right] - \frac{\partial p}{\partial r}, \quad [2.1.1.6]$$

$$\frac{\partial v}{\partial t} + u\frac{\partial v}{\partial r} + v\frac{\partial v}{\partial z} = \frac{1}{\mathrm{Re}}\left[\frac{\partial^2 v}{\partial r^2} + \frac{\partial^2 v}{\partial z^2} + \frac{1}{r}\frac{\partial v}{\partial r}\right] - \frac{\partial p}{\partial z} - \frac{1}{\mathrm{Fr}^2},$$

$$\frac{\partial T}{\partial t} + u\frac{\partial T}{\partial r} + v\frac{\partial T}{\partial z} = \frac{1}{\mathrm{Pe}}\left[\frac{\partial^2 T}{\partial r^2} + \frac{\partial^2 T}{\partial z^2} + \frac{1}{r}\frac{\partial T}{\partial r}\right], \quad [2.1.1.7]$$

$$\frac{\partial T}{\partial t} = \frac{1}{\mathrm{Pe}}\left[\frac{\partial^2 T}{\partial r^2} + \frac{\partial^2 T}{\partial z^2} + \frac{1}{r}\frac{\partial T}{\partial r}\right], \quad [2.1.1.8]$$

where the above equation is obtained by setting the velocities to zero in the thermal energy equation (2.1.1.7).

The idea behind the non-dimensionalization of the governing differential equation is to get a feel for the dominant physical phenomenon that exists in the process. For example, in the stand-alone equation for heat conduction (pure diffusion) in a solid, the Fourier number is the non-dimensionalized time. When the thermal energy equation for the liquid melt defaults to that for the solid when the velocity components become zero, however, the coefficient of the diffusion term, i.e., the reciprocal of the Peclet number is carried over. This makes the dimensionless time in the solid heat conduction to be the product of Peclet and Fourier numbers, since the dimensionless time is arrived at based on convection and not on pure conduction. Besides providing insight into the various physical processes that take place, the non-dimensionalized numbers can be used as parameters for input in the numerical simulation process, i.e., the dimensionless kinematic viscosity and thermal diffusivity which are the reciprocals of Re and Pe, respectively, and the dimensionless time which is the F_0 only need be changed to simulate drilling in a different material with different thermophysical properties, besides changing the Weber number (the reciprocal of the dimensionless surface tension coefficient) in the input data.

2.1.2. *Gas Dynamics*

The model used in this study to obtain the temperature and pressure at the liquid layer surface is an extension of

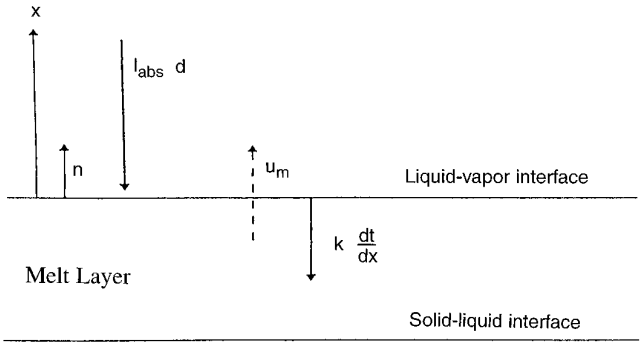

FIG. 2. Energy balance in the moving coordinate system. Part of the absorbed incident laser energy flux is conducted into the melt and the rest of it is forms the latent heat of evaporation of the melt.

an earlier model by von Allmen [7] which assumes the temperature to be continuous across the melt/vapor interface. In a non-equilibrium situation, the melt surface properties are determined from the conservation of mass, momentum, and energy fluxes across the melt/vapor interface. Relative to the lab frame, the velocity at which the melt surface moves will be denoted by $\vec{\mathbf{v}}_{lv}$, and the velocities of the melt and vapor will be denoted by $\vec{\mathbf{v}}_m$ and $\vec{\mathbf{v}}_v$, respectively. In what follows, a local coodinate system will be constructed which rides with the melt surface element, with $\hat{\mathbf{n}}$ as the unit vector outward normal to the surface element. In the local moving frame the velocities of the melt and vapor leaving the melt surface will be denoted by $\vec{\mathbf{u}}_m$ and $\vec{\mathbf{u}}_v$, respectively. These velocities are related by

$$\vec{\mathbf{u}}_m = \vec{\mathbf{v}}_m - \vec{\mathbf{v}}_{lv}, \quad \vec{\mathbf{u}}_v = \vec{\mathbf{v}}_v - \vec{\mathbf{v}}_{lv}. \qquad [2.1.2.1]$$

Nomenclature will be adopted in which the temperatures at the melt surface, in the vapor and in the melt will be denoted as T_s, T_v, and T_m, respectively. By assumption, taking T_v and T_m very close to the melt surface gives $T_s \equiv T_m \equiv T_v$.

In the moving frame, mass, momentum, and the energy balances across the melt/vapor interface may be written as [11]

$$\rho_m \vec{\mathbf{u}}_m \cdot \hat{\mathbf{n}} = \rho_v \vec{\mathbf{u}}_v \cdot \hat{\mathbf{n}} \qquad [2.1.2.2]$$

$$p_m \hat{\mathbf{n}} + \rho_m \vec{\mathbf{u}}_m (\vec{\mathbf{u}}_m \cdot \hat{\mathbf{n}}) = P_v \hat{\mathbf{n}} + \rho_v \vec{\mathbf{u}}_v (\vec{\mathbf{u}}_v \cdot \hat{\mathbf{n}}) \qquad [2.1.2.3]$$

$$I\hat{\mathbf{d}} \cdot \hat{\mathbf{n}} + L_v \rho_v \vec{\mathbf{u}}_v \cdot \hat{\mathbf{n}} + k \nabla T|_s \cdot \hat{\mathbf{n}} = 0, \qquad [2.1.2.4]$$

where $\nabla T|_s$ is the temperature gradient in the melt just below the melt/vapor interface which is a positive quantity refering to Fig. 2. Some studies in the literature indicate that the gas velocity leaving the surface is nearly sonic [12] at the laser intensities typical of laser drilling. The nonequilibrium phase of the gas in the Knudson layer does not allow a unique assignment of temperature and thus in general there could be a discontinuity in temperature between the vapor and melt. However, we assumed $T_v = T_s$ for simplicity near the melt/vapor interface and ideal gas behavior in the vapor which lead to the approximation $\mathbf{v}_v \simeq c = \sqrt{\kappa R T_s}$, where $\mathbf{v}_v = |\vec{\mathbf{v}}_v|$. Since $\mathbf{v}_v \gg |\vec{\mathbf{v}}_{lv}|$ and $\rho_m \gg \rho_v$, Eq. (2.1.2.2) implies $u_v \gg u_m$ and $u_v \simeq \mathbf{v}_v$, leading to

$$u_v \simeq \sqrt{\kappa R T_s}. \qquad [2.1.2.5]$$

Previous calculations of the temperature gradient in the melt show that the tangential component along the melt/vapor interface is negligible compared to the normal component, [13] and the approximation can be made that $\vec{\mathbf{u}}_v$ (and thus $\vec{\mathbf{u}}_m$) are normal to the melt/vapor interface. Thus equations (2.1.2.2)–(2.1.2.4) can be written in one dimension as

$$\rho_m u_m = \rho_v u_v \qquad [2.1.2.2a]$$

$$p_m + \rho_m u_m^2 = p_v + \rho_v u_v^2 \qquad [2.1.2.3a]$$

$$I_{\text{abs}} - L_v \rho_v u_v - k \frac{\partial T}{\partial n} = 0, \qquad [2.1.2.4a]$$

where I_{abs} is the rate of energy absorption, $u_m \equiv |\vec{\mathbf{u}}_m|$, $u_v \equiv |\vec{\mathbf{u}}_v|$, $\partial T/\partial n$ is the temperature gradient in the melt just below the melt/vapor interface in the direction normal to the interface. The system of equations is completed using the ideal gas law $p_v = R\rho_v T_v$ and the Clausius/Clapeyron equation [14]

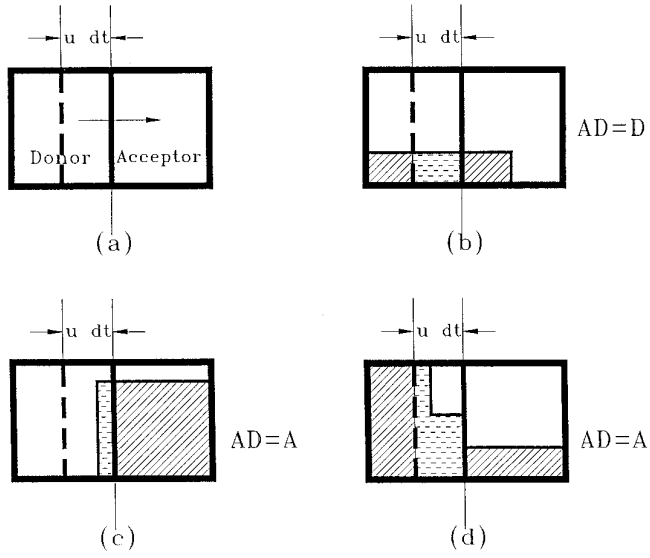

FIG. 3. Fluxing rules in donor–acceptor cell method.

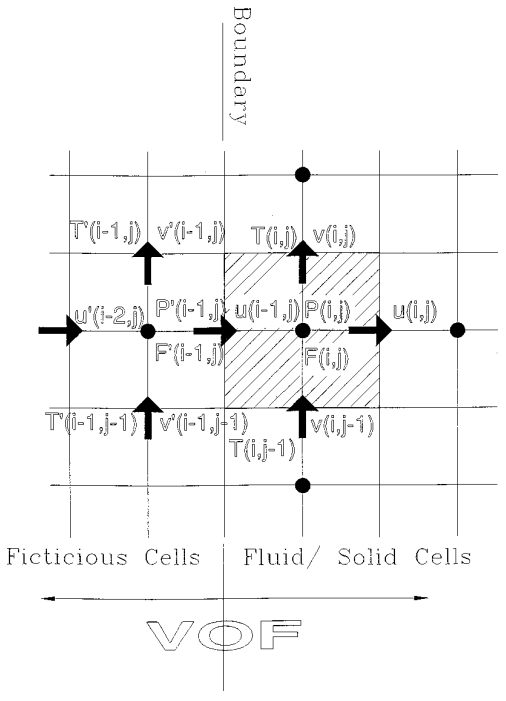

FIG. 4. Placement of field variables and fictitious cell. A typical cell is cross hatched. The variables, pressure p, and the volume of fluid function F are the center. The r-direction velocity components are located at the center of right and left edges, whereas the z-direction velocity components are located at the center of top and bottom edges. The fictitious cell variables are differentiated with a prime.

$$p(T_s) = p_{\text{vap},0} \exp\left[\frac{L_v}{R}\left(\frac{1}{T_{\text{vap},0}} - \frac{1}{T_s}\right)\right]. \quad [2.1.2.6]$$

The surface properties may be obtained as follows. Using (2.1.2.2a) and (2.1.2.3a) and noting that $\rho_m \gg \rho_v$ gives

$$p_m = p_v + \left(1 - \frac{\rho_v}{\rho_m}\right)\rho_v u_v^2 \simeq p_v + \rho_v u_v^2. \quad [2.1.2.7]$$

Equation (2.1.2.7) may be combined with (2.1.2.5) to give

$$p_m = R\rho_v T_v(1 + \kappa), \quad [2.1.2.8]$$

ρ_v may be found from (2.1.2.4a) as

$$\rho_v = \left(I_{\text{abs}} - k\frac{\partial T}{\partial n}\right)\left(L_v\sqrt{\kappa R T_s}\right)^{-1}$$

which may be substituted into (2.1.2.8) to give

$$p_m = \frac{\kappa + 1}{L_v \kappa}\sqrt{\kappa R T_s}\left(I_{\text{abs}} - k\frac{\partial T}{\partial n}\right). \quad [2.1.2.9]$$

Identifying the surface pressure to be used in the fluid calculations as being the pressure just below the melt/vapor surface ($p_m = p_s$) and using $T_s \equiv T_v$ at the melt/vapor surface, Eqs. (2.1.2.6) andd (2.1.2.9) may be combined to give

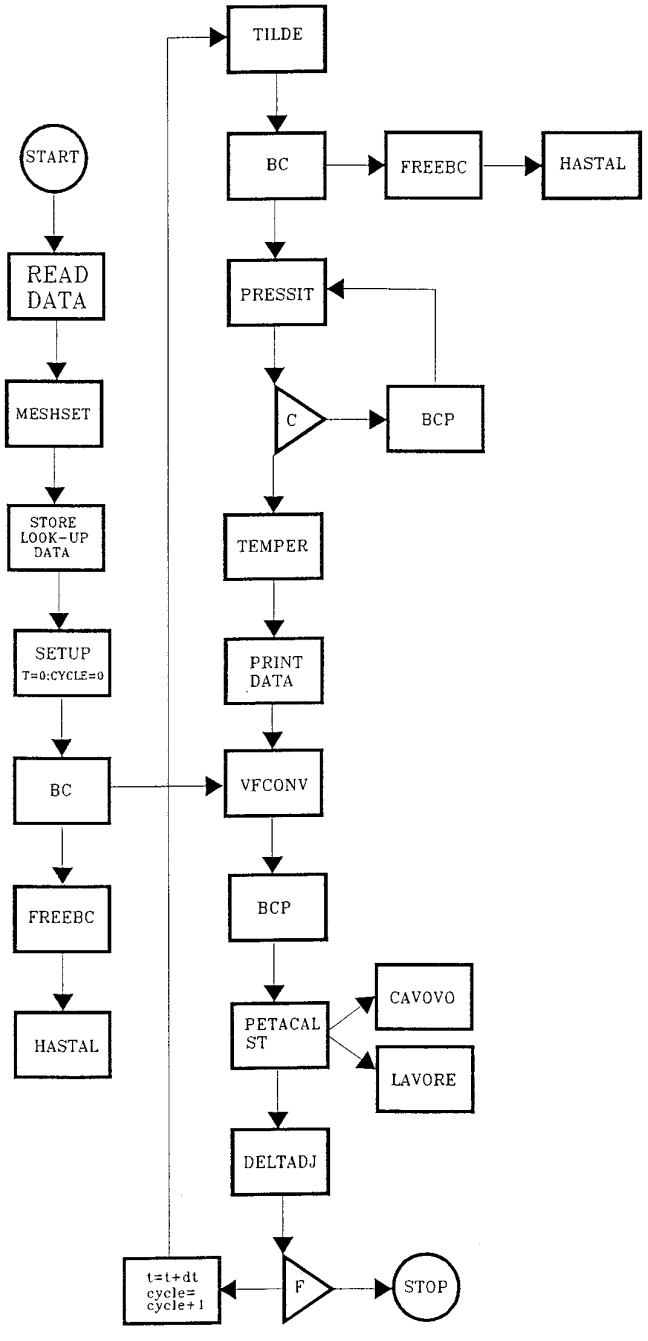

FIG. 5. Flow chart of SOLA-LAD. The figure shows all the subroutines sequentially and in the loop. There is a cycle loop and within this lies the pressure iteration loop. The termination criterion is based on the time to finish.

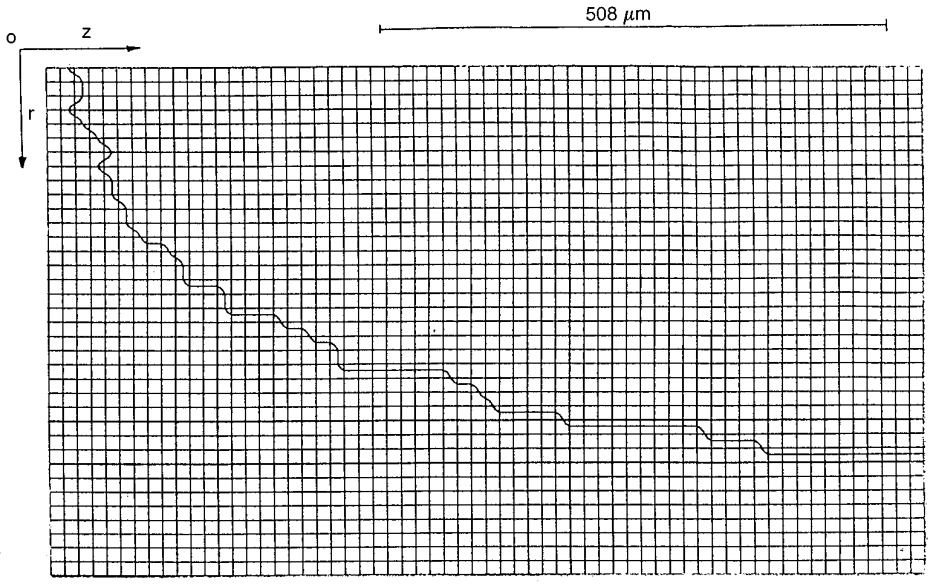

FIG. 6. Discretized solid–liquid interface. The figure is rotated 90° anti-clockwise so that the z-axis coincides with the horizontal with the origin at the top-left hand corner. The positive radial direction is vertically downward from the origin. The contour plotting algorithm has drawn the line in an average sense demarcating the solid from the rest.

$$\frac{\kappa+1}{L_v\kappa}\sqrt{\kappa R T_s}\left(I_{\text{abs}}+k\frac{\partial T}{\partial n}\right) = p_{\text{vap},0}\exp\left[\frac{L_v}{R}\left(\frac{1}{T_{\text{vap},0}}-\frac{1}{T_s}\right)\right]. \quad [2.1.2.10]$$

In practice Eq. (2.1.2.10) is evaluated for two cases. At higher beam intensities $I_{\text{abs}} \gtrsim 0.1$ MW/cm^2) heat conduction into the melt is small compared to the rate of energy absorption and the temperature gradient term $\partial T/\partial n$ may be neglected. In this limit T_s and p_s respond instantly to changes in I_{abs}. At lower beam intensities the flow velocity of the vapor is small, and neglecting u_v in Eq. (2.1.2.4a) gives the approximation $\partial T/\partial n = I_{\text{abs}}/k$. In both cases T_s and p_s are determined as functions of the absorbed beam intensity.

2.2 Assumptions

The assumptions made in the theoretical model comprising heat transfer, fluid mechanics, and gas dynamics are:

1. The incident beam is normal to the original surface of the irradiated material and the analysis may be done as an axisymmetric 2D problem.

2. Thermophysical properties remain constant and they are the same in the melt and solid regions.

3. The target material is assumed to behave as a pure substance and the temperature of melting is well defined.

4. The vapor behaves as an ideal monatomic gas in the gas dynamics model.

5. The reflectivity of the target material at temperatures near vaporization is taken to be zero.

6. Thermalization of the incident laser energy is taken to be instantaneous and the surface temperature changes occur quickly compared to the changes in the hole geometry.

7. There is no plasma formation, the vapor is transparent to the incident laser radiation, and the light scattering due to ejected melt can be neglected.

8. The laser beam varies with both position and time in a Gaussian sense and may have multiple peaks.

3. NUMERICAL FEATURES OF THE CODE

3.1. SOLA-LAD

The algorithm for laser drilling is a modification of solution algorithm for volume of fluid (SOLA-VOF) method which uses a type of donor–acceptor flux approximation. Figure 3 shows examples of free-surface shapes used in the advection of F. The donor-acceptor arrangement is illustrated in (a), where the dashed regions shown in (b–d) are the actual amounts of F fluxed. $V_x = udt$, $df = \min\{F_{AD}|V_X| + CF, F_D\, dX_D\}$, where $CF = \max\{(1.0 - F_{AD})|V_X| - (1.0 - F_D)\, dX_D, 0.0\}$. Special care is taken to preserve the sharp definition of free boundaries. Standard finite-difference approximations are inadequate to handle the volume of fluid function F and interfaces cannot be sustained. F moves with the fluid and the time dependence of F is governed by the equation

TABLE I

Material Properties of Hastelloy-X

Property	Symbol	Value
Density	ρ	8.4 g cm^{-3}
Thermal conductivity	k	0.217 J cm^{-1} s^{-1} °K^{-1}
Thermal diffusivity	α	0.042 cm^2 s^{-1}
Specific heat	c_p	0.610 J g^{-1} K^{-1}
Temp of vaporization	$T_{v,0}$	3100 °K
Temp of melting	T_m	1510 °K
Latent heat of vapor	L_v	6444 J g^{-1}
Latent heat of melt	L_m	231 J g^{-1}
Molar mass	M	76 g mole^{-1}
Dynamic viscosity	μ	0.5 g cm^{-1} s^{-1}
Surface tension	γ	0.0001 J cm^{-2}

$$\frac{\partial F}{\partial t} + u\frac{\partial F}{\partial r} + v\frac{\partial F}{\partial z} = 0. \qquad [3.1]$$

which is solved along with the field equations of Section 2.1. F is unity for a full fluid cell and zero for an empty cell. F is a step function which permits and preserves the nature of the donor–acceptor flux approximation method. VOF technique follows regions rather than boundaries through an Eulerian mesh of stationary cells. The value of F upstream and downstream of a flux boundary is used to establish a crude interface shape which is then used to compute the flux across the boundary. This method uses pressure and velocity as the primary dependent variables. A free surface cell is a cell containing a nonzero value of F and having at least one neighboring cell that contains a zero value of F. For donor cell form, the weighting for the upstream and downstream derivatives are 2 and 0, respectively. The donor cell and the centered difference approximation is combined into a single expression with a parameter that controls the relative amount of each. The velocities appearing in the field equations evaluated at the new $n + 1$ time interval depend on the pressure in the momentum equation occurring at the same $n + 1$ time interval. Therefore, this equation is an implicit relation for the new pressure. The pressure iteration is carried out using the continuity equation until the implicit relationship for pressure and velocity is satisfied for all the full cells and also in such a way that the pressures in all free surface cells satisfy the applied surface pressure. When the free surface boundary conditions are being applied the conservation of mass is enforced for the free surface cells. Near the walls, adhesion effects are taken into account which requires the specification of the contact angle.

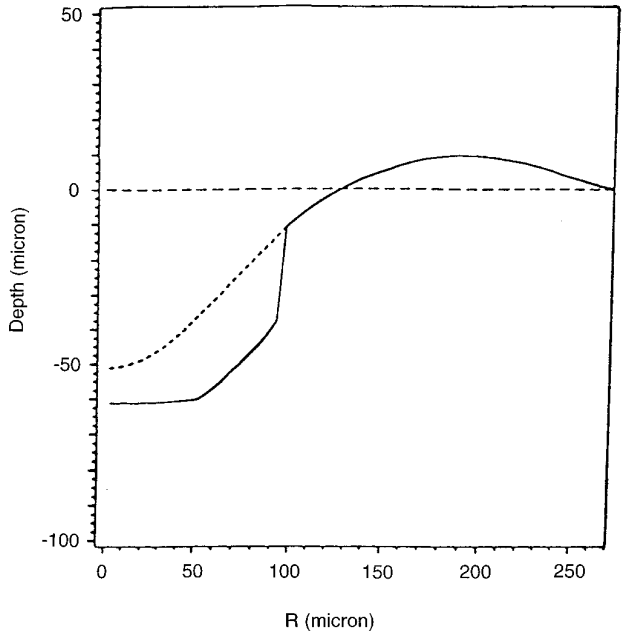

FIG. 7. Laser drilling simulation at 200 μs without recast. The beam profile is given in Section 4.1. The dotted line represents the melt surface and the solid line represents the surface where $T = T_{\text{melt}}$. Recast is not on.

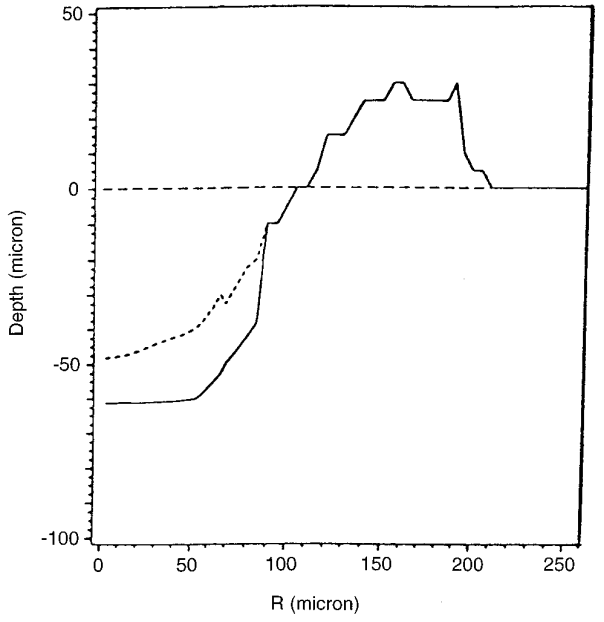

FIG. 8. Laser drilling simulation at 200 μs with recast. The beam profile is given in Section 4.1. The dotted line represents the melt surface and the solid line represents the surface where $T = T_{\text{melt}}$. Recast is on.

3.2. Boundary Conditions

It is required to set proper boundary conditions at all mesh boundaries, surfaces of all internal obstacles, and the free surface boundary.

3.2.1. *Mesh Boundaries*

The placement of the field variables and the fictitious cells outside the fluid side are shown in Fig. 4. At the mesh

TABLE II

Simulated Runs

No.	n	I_0 Mw/cm^2	T_{fin} μs	t_{pn} μs	t_d μs	r_d μm
1	1	1.65	1300	300	300	127
2	1	3.3	1200	300	300	127
2a	1	3.3	1200	300	300	127
3	1	3.3	1200	300	300	180
4	1	3.3	1200	500	500	127
5	1	6.7	1300	300	300	127
6	1	10	1200	300	300	127
7	1	10	1200	500	500	127
8a	1	5	3300	300	300	127
8b	2	5	3300	1300	300	127
9a	1	20	3300	300	300	127
9b	2	20	3300	1300	300	127

boundaries of the physical model, a layer of fictitious cells surrounding the mesh is used to enforce different boundary conditions. Assume for demonstration purposes, the boundary between the fictitious column of cells and the fluid/solid column of cells as shown in Fig. 4 to be the axis of the cylindrical region in the axisymmetric problem. This boundary will act like a rigid-slip wall; hence the normal velocity must be zero and the tangential velocity should have no normal gradient, i.e. (setting $i = 2$ in Fig. 4).

$$u_{1,j} = 0.0, \qquad v_{1,j} = v_{2,j} \quad \forall j. \qquad [3.2.1.1]$$

If the same left boundary is treated as a no-slip rigid wall, then the tangential velocity component at the wall should also be zero, i.e. (setting $i = 2$ in Fig. 4),

$$u_{1,j} = 0.0, \qquad v_{1,j} = v_{2,j} \quad \forall j. \qquad [3.2.1.2]$$

For the pressure and volume of fluid function F (explained in Section 3.1), the boundary conditions are

$$p_{1,j} = p_{2,j}, \qquad F_{1,j} = F_{2,j} \quad \forall j. \qquad [3.2.1.3]$$

These conditions are imposed on the velocities computed from the momentum equations and also after each pass through the mesh, during pressure iteration. For tempera-

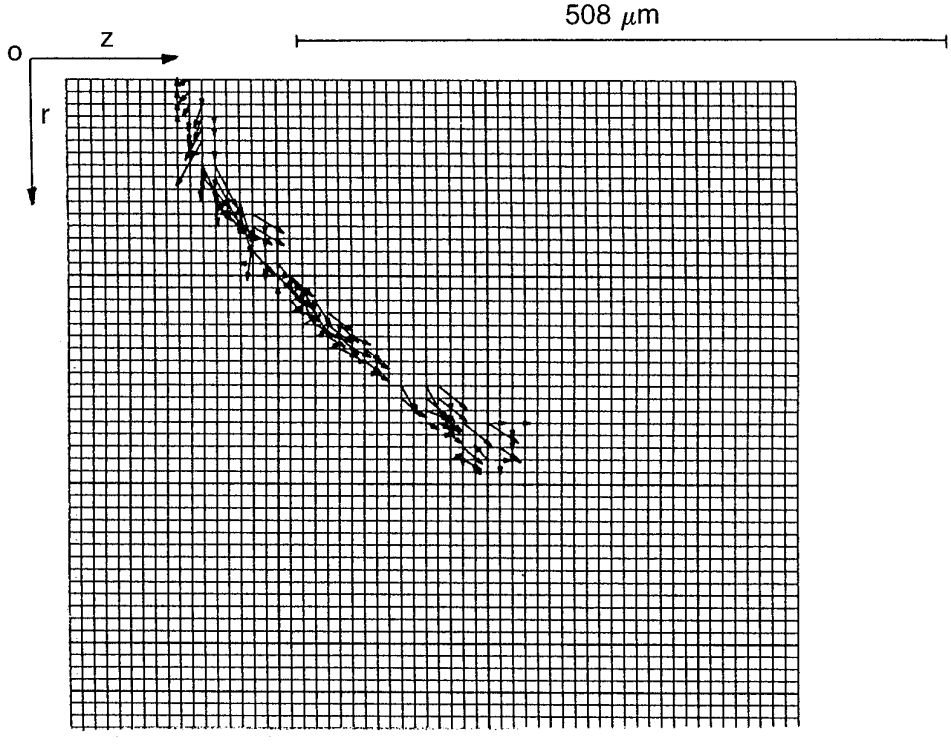

FIG. 9. Velocity vector plot at 600 μs for case 6. The figure is rotated 90° anti-clockwise so that the z-axis coincides with the horizontal with the origin at the top left-hand corner. The positive radial direction is vertically downward from the origin. The velocity vectors show the movement of melt radially outward along the incline. The plotting algorithm uses an averaging of velocity components and the node is actually the center of a cell. Each cell is approximately 10 by 10 microns. The scale is shown in the top right-hand corner.

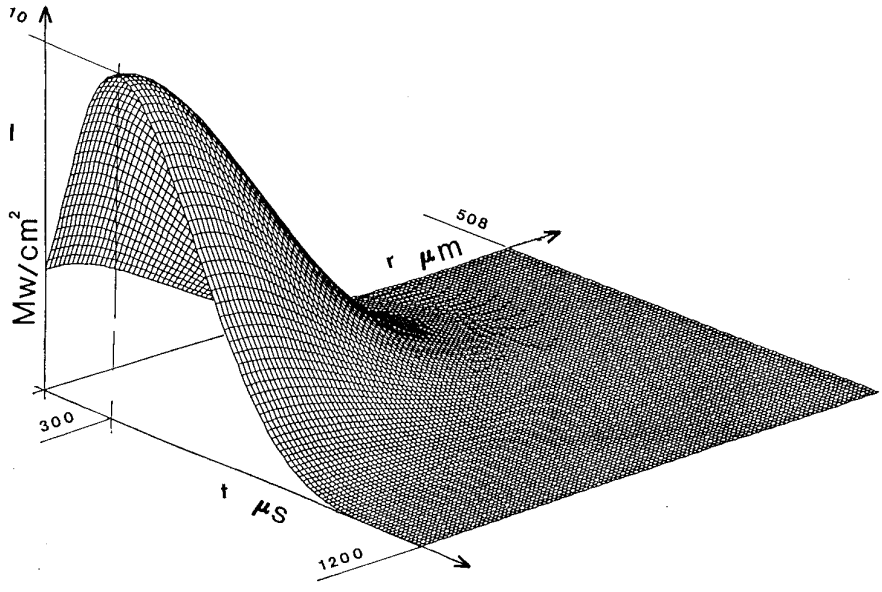

FIG. 10. Typical laser beam intensity profile. The figure shows the spatial and temporal variations of the laser beam for the simulated run (case 6) listed in Table II. The intensity is plotted on the vertical axis and the horizontal plane has t (time coordinate) and r (radial coordinate) as axes. There is a peak occurring at 300 μs. It can also be observed the intensity is symmetric with respect to the origin spatially at all times in the I-r plane.

ture, the peripheral boundaries have zero temperature gradient boundary conditions. Assume the boundary shown in Fig. 4 to be the left peripheral boundary, then (setting $i = 2$ in Fig. 4) the condition is enforced as

$$T_{1,j} = T_{2,j} \quad \forall j. \qquad [3.2.1.4]$$

The temperature boundary conditions are imposed on the temperature computed from the thermal energy equation. Since the thermal energy equation resembles the z-momentum equation, the location of the temperature grid points are chosen to be the same as that of z-component of velocity.

3.2.2. *Free Surface Boundary*

The free surface boundary condition for the pressure is accomplished by setting the surface cell pressure equal to the value obtained by a linear interpolation between the pressure wanted at the surface (which is the sum of the pressure computed by the gas dynamics model and the pressure due to surface tension effect) and the pressure in the adjacent full fluid cell. The pressure due to the surface tension effect is obtained by the product of the local curvature of the boundary cell and the surface tension coefficient (Table I):

$$\begin{aligned} p_{\mathrm{st}} &= -\gamma K_c \\ K_c &= K_{XY} + K_{\mathrm{CYL}} \qquad [3.2.2.1] \\ &= \frac{1}{R_{XY}} + \frac{1}{R_{\mathrm{CYL}}} \end{aligned}$$

For a sufficiently high absorbed laser beam intensities ($I_{\mathrm{abs}} \geq 0.1$ MW/cm^2) heat conduction into the melt is small compared to the rate of energy absorption (which is more or less equal to the energy going into the latent heat of vaporization). For lower beam intensities, however, the latent heat can be neglected and almost all the energy is conducted into the metal. [15] In either case the temperature boundary condition for the melted pool surface as given by the gas dynamics model is

$$T = T_v(\vec{r}, t; I_{\mathrm{abs}}), \qquad [3.2.2.2]$$

where T_v is the vaporization temperature which depends on the position, time, and the absorbed laser intensity. In principle a similar flux boundary condition should exist at the liquid–solid interface, but since the latent heat of melting L_m is many folds smaller [3] compared of L_v and the temperature gradients are large, a constrained (Dirichlet) temperature boundary condition that of melting temperature is in order when the thermal conductivities in the melt and the solid are assumed to be the same. Hence, at the solid–liquid interface the implicit temperature boundary condition is

$$T = T_m, \qquad [3.2.2.3]$$

where T_m is the temperature of melting. Outside the range of the laser beam, however, zero temperature gradient boundary condition is applied.

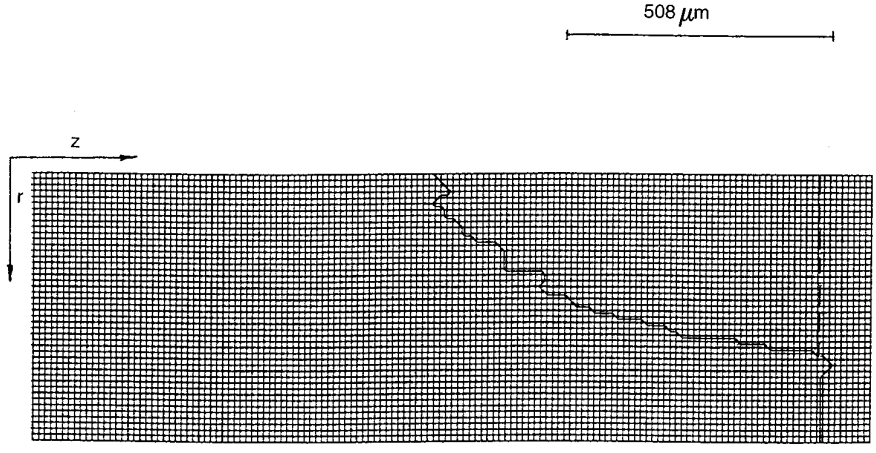

FIG. 11. Hole drilled for test case 6. The figure is rotated 90° anti-clockwise so that the z-axis coincides with the horizontal with the origin at the top left-hand corner. The positive radial direction is vertically downward from the origin. Each cell is approximately 10 by 10 microns. The scale is shown in the top right-hand corner. The figure shows the solid metal with a recast formed at the outer periphery. The vertical dotted line shows the initial metal surface before drilling.

3.3. Algorithm Implementation

The flow chart of the algorithm employed in the numerical simulation of the laser drilling process is shown in Fig. 5. The modifications made in the original SOLA-VOF to model the laser drilling process are explained subroutine-wise (single * indicates a modified subroutine, whereas a ** indicates a new one).

1. *READ DATA**
   Input data consists of non-dimensionalized thermophysical properties, boundary condition flags, print time interval, time to finish simulation, etc., and the mesh data. Special flags, such as the one for turning on the recast are not present in the original SOLA-VOF.
2. *MESHSET*
   The coordinates of the grid points and the center of the cells are calculated and stored in arrays.
3. *LOOK-UP DATA***
   A look-up table comprising the temperature and pressure values corresponding to the laser intensity as calculated by a gas dynamics model is read and stored in memory and accessed from the subroutine HASTAL whenever the free surface boundary conditions are applied once in every cycle.
4. *SETUP**
   The initial conditions at $t = 0$ and cycle $= 0$ are set up in this subroutine. Ambient temperature and pressure and solid configuration are some of the initial conditions.
5. *BC**
   The boundary conditions are applied on the fixed and free boundaries of the mesh during every cycle. FREEBC is called for the application of temperature and pressure free boundary conditions. Temperature is applied on the cell grid point, whereas the pressure is applied to the whole region column-wise, which stays in effect for the entire cycle, until it is reassigned in this subroutine in the subsequent cycle.
6. *FREEBC***
   This is a new subroutine that was not present in the original SOLA-VOF. The free temperature and pressure, as well as the temperature gradient boundary conditions, are applied on the liquid (liquid–vapor) and solid (solid–vapor) free boundaries. Subroutine HASTAL is called to access the values which are read into the memory earlier.
7. *HASTAL***
   This is a new subroutine which accesses values from the look-up table in the memory and feeds them to FREEBC. The temperature gradient values can also be calculated when appropriate.
8. *TILDE*
   This calculates the explicit solution for each of the momentum equations; i.e., the new time $n + 1$ values of velocities are obtained from the time n values of pressure, advective, and diffusive accelerations. These values will be advanced to time $n + 1$ values in the pressure interation in PRESSIT.
9. *PRESSIT*
   Iterates velocity and pressure fields such that mass is conserved in each cell of the mesh. The first guess value is the one obtained from the subroutine TILDE. The free surface cell pressure is adjusted to comply with the applied surface pressure in the region. The

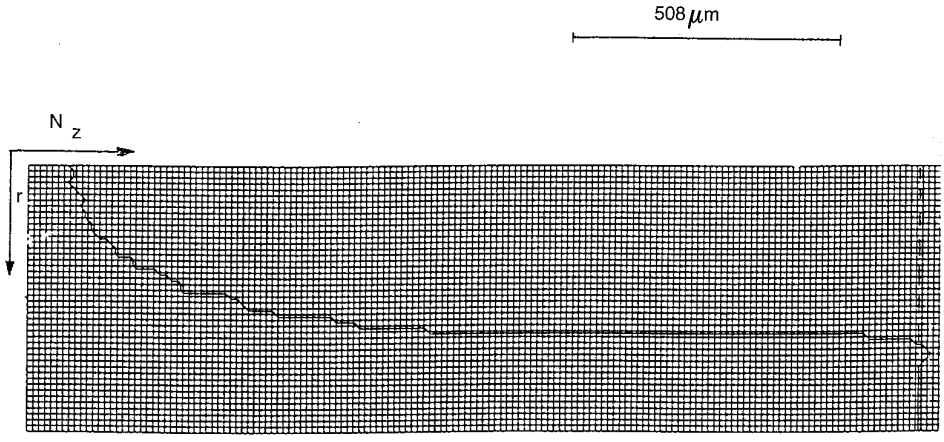

FIG. 12. Hole drilled for test case 7. The figure is rotated 90° anti-clockwise so that the z-axis coincides with the horizontal with the origin at the top left-hand corner. The positive radial direction is vertically downward from the origin. Each cell is approximately 10 by 10 microns. The scale is shown in the top right-hand corner. The figure shows the solid metal with a recast formed at the outer periphery. The vertical dotted line shows the initial metal surface before drilling. The hole has become deeper and steep along the sides.

mass conservation in the surface cells is not iterated upon, but is enforced in the free surface boundary condition in the subroutine BCP.

10. *BCP*
Same as BC with no application of temperature and pressure boundary conditions at the free surface. The surface pressure assigned to the region in BC still stays in effect.

11. *TEMPER***
This subroutine is the most important of all the subroutines in the laser drilling simulation and it is entirely new. The velocity and the pressure fields obtained in PRESSIT implicitly satisfy the continuity and momentum equations. For the given velocity field, the temperature field can now be obtained by treating the thermal energy equation Eq. (2.1.1.7) as an advection–diffusion equation; i.e., the left-hand side of the equation is the substantial derivative of temperature. Mathematically, the Navier–Stokes equation is a quasi-linear equation, whereas the thermal energy equation is a linear one which needs no iteration for the consistent solution. The thermal energy equation is discretized in the same fashion as the z-momentum equation. Here, the cells are swept from bottom to top column-wise and, depending upon whether the average temperature of the cell is below or above the melting temperature, the cell is turned into either an obstacle (solid) cell or a full fluid cell. Therefore, the accuracy of this type of modeling is only as good as the discretization of the mesh. Whenever the melt is ejected or separated from the molten pool, the cell occupying the separated fluid droplet is made empty while keeping track of the total amount of fluid thus lost. This is done not to interfere with the temperature and pressure boundary conditions which would be applied only on the contiguous free surface.

12. *VFCONV**
This integrates the convection of the volume of fluid F in Eq. (3.1). Any loss or gain of F during this integration process is kept track of.

13. *PETACAL**
The slope of the surface in the surface cells, the cell flag which indicates the interpolation neighbor for surface cell pressure calculation and the surface pressure due to surface tension effect are determined.

14. *CAVOVO**
Calculates the volume of void regions.

15. *LAVORE**
Detects and labels all void regions.

16. *PRTPLT**
The desired output is printed at the desired time.

17. *DELTADJ**
Computes maximum allowable Δt obeying the stability criteria. Adjusts Δt whenever convection limit is exceeded in VECONV or the maximum number of pressure iteration is exceeded in *PRESSIT*.

As the simulation progresses, the location of the melt, the velocity field of the melt, the temprature field in the liquid and the solid phases, and the pressure distribution are obtained. The melting and solidification is modeled using a switch-on switch-off technique. The melting of a cell is simulated by ''turning'' on an obstacle cell once its average temperature becomes higher than the melting temperature by setting the ''F'' function in that cell equal to unity and thereby treating that cell as a fluid cell. In the same fashion, solidification is simulated by ''turning'' off

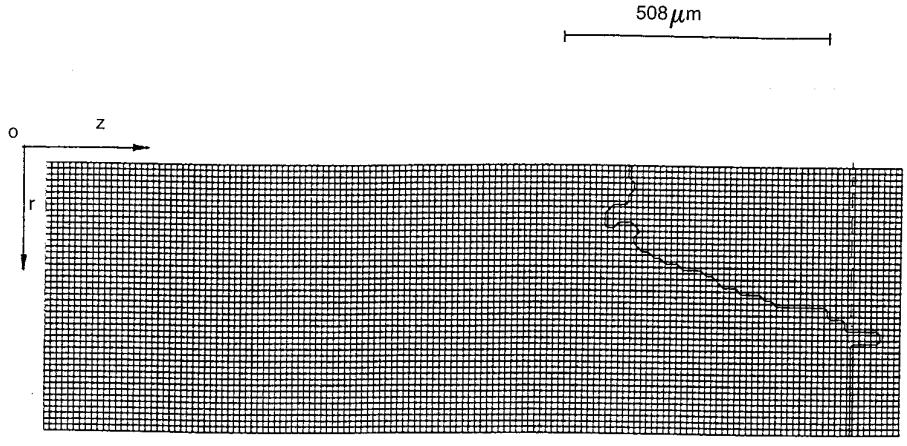

FIG. 13. Hole drilled for test case 8a. The figure is rotated 90° anti-clockwise so that the z-axis coincides with the horizontal with the origin at the top left-hand corner. The positive radial direction is vertically downward from the origin. Each cell is approximately 10 by 10 microns. The scale is shown in the top right-hand corner. The figure shows the solid metal with a recast formed at the outer periphery. The vertical dotted shows the initial metal surface before drilling.

a fluid cell into an obstacle cell when the average temperature of that cell falls below that of melting. The effect of material removal by direct vaporization is effected by adjusting the values of F in each cell. Thus the free surface boundary (liquid–vapor interface) and the moving boundary (solid–liquid interface) which are obtained self-consistently as parts of the solution will be represented by series of steps consisting of the cell boundaries closest to the interfaces as depicted in Fig. 6. The implementation of the algorithm can be broadly summarized as follows:

1. Calculate (by means of the gas dynamics model) and apply the pressure and temperature surface boundary conditions which are functions of the incident laser beam intensity corrected for the orientation of the target surface. Symmetry and no-slip boundary conditions are applied for velocity components. Symmetry and insulated boundary conditions are applied for the temperature.

2. Solve for velocity field, pressure field, free surface (liquid–vapor interface), and moving boundary (liquid–solid interface). The time step in the program is automatically adjusted to satisfy all fluid stability criteria.

3. The temperature field is then obtained by solving the advection–diffusion thermal energy equation for the obtained velocity field.

4. The temperature field is used to turn the cell into

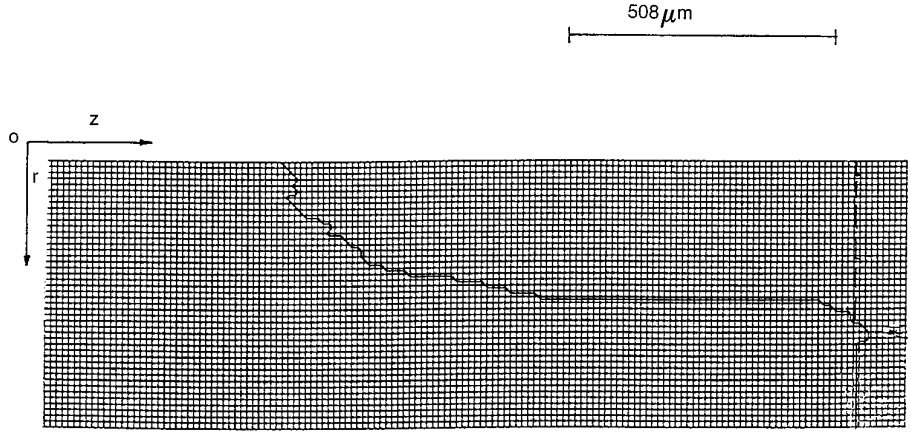

FIG. 14. Hole drilled for test case 8b. The figure is rotated 90° anti-clockwise so that the z-axis coincides with the horizontal with the origin at the top left-hand corner. The positive radial direction is vertically downward from the origin. Each cell is approximately 10 by 10 microns. The scale is shown in the top right-hand corner. The figure shows the solid metal with a recast formed at the outer periphery. The vertical dotted line shows the initial metal surface before drilling.

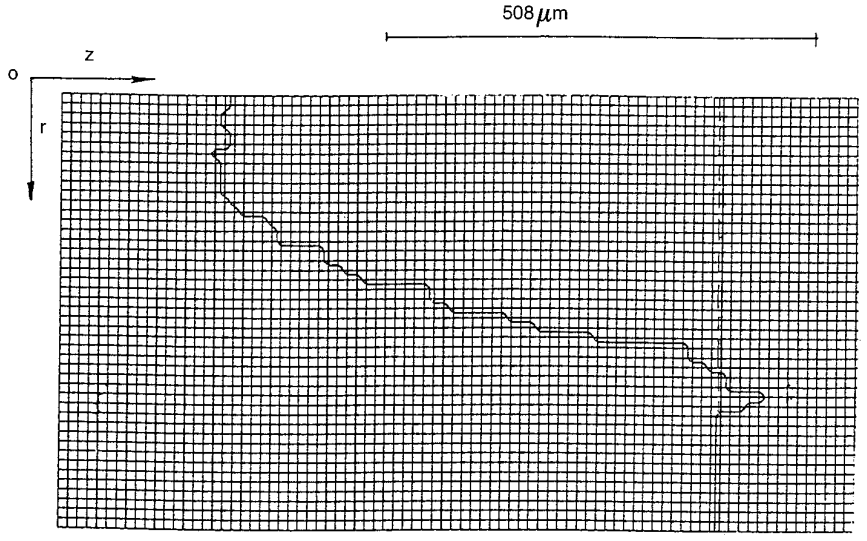

FIG. 15. Hole drilled for test case 9a. The figure is rotated 90° anti-clockwise so that the z-axis coincides with the horizontal with the origin at the top left-hand corner. The positive radial direction is vertically downward from the origin. Each cell is approximately 10 by 10 microns. The scale is shown in the top right-hand corner. The figure shows the solid metal with a recast formed at the outer periphery. The vertical dotted line shows the initial metal surface before drilling.

liquid or a solid by comparing the average temperature of the cell with the melting temperature.

5. Return to step 1 and cycle until the time to finish is reached.

4. RESULTS AND DISCUSSION

The computer code that has been developed and discussed in detail is used to generate useful information that enables one to get quantitative, as well as qualitative, comparisons with actual experimental observations. This section presents such simulated results wherein a Gaussian beam profile in space and time is assumed as given by

$$I(r,t) = I_0 \exp\left\{-\frac{(r-r_p)^2}{r_d^2}\right\} \sum_{n=1}^{N} \exp\left\{-\frac{(t-t_{pn})^2}{t_d^2}\right\}, \qquad [4.1]$$

where, r_d and t_d are the damping radii in space and time for the laser beam. The nth peak intensity occurs at time t_{pn} and in space at r_p. For the axisymmetric problem r_p is zero because the origin is located at the center, where the maximum intensity occurs in space. The energy delivered to the target is given by

$$E = \int_0^t dt' \int_0^R I(r',t')\,(2\pi r')\,dr' \qquad [4.2]$$

and the total maximum power delivered by the beam at the temporal peak intensity is given by

$$P_{\max} = \pi r_d^2 I_0 \left[1 - \exp\left\{-\frac{R^2}{r_d^2}\right\}\right], \qquad [4.3]$$

where R is taken to be 508 μm. The target material used was Hastelloy-X for the simulation and Table I lists the properties.

4.1. Effects of Recast Formation

The effect of resolidification (recast) of the flowing melt on the resulting hole geometry was also studied and found to be significant. Two simulations were done, one with and the other without the recast formation, uisng the beam profile described below. The peak intensity of the beam was taken to be $I_0 = 0.35$ MW/cm^2. The time at which the peak occurred was $t_p = 50$ μs, the time decay factor was taken as $t_0 = 50$ μs, the radial decay factor was $r_0 = 72$ mu and the beam was cut off beyond the radius 254 μm.

The results of simulations are shown in Fig. 7 and Fig. 8. In both simulations, the solid was allowed to melt when the temperature went above the melting point T_{melt}. As the temperature fell below T_{melt}, solidification occurred in the simulation with recast but was not allowed to occur in the simulation without recast. Thus in the no-recast simulation, once the material is melted it was treated as a liquid for the duration of the simulation, even for temperatures below T_{melt}. In both simulations a no-slip boundary was imposed at the melt/solid interface.

The recast formation affects the crater geometry in two ways. Without recast the crater would eventually fill back

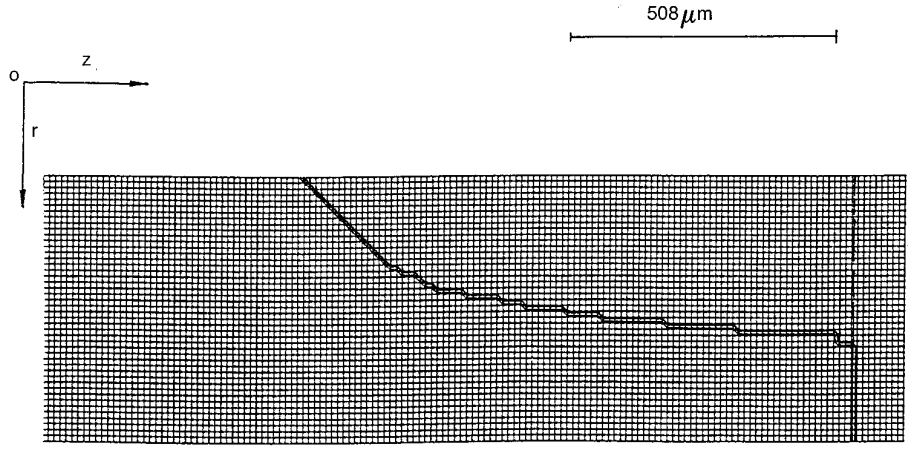

FIG. 16. Hole drilled for test case 9b. The figure is rotated 90° anti-clockwise so that the z-axis coincides with the horizontal with the origin at the top left-hand corner. The positive radial direction is vertically downward from the origin. Each cell is approximately 10 by 10 microns. The scale is shown in the top right-hand corner. The figure shows the solid metal with a recast formed at the outer periphery. The horizontal surface shows the initial metal surface before drilling.

up (either fully or partially) due to gravity and surface tension pulling the ejected fluid back into the crater. The other effect is due to the hump barrier at the outer edge of the hole. The melt flow characteristics are influenced even at early times by the formation of the hump and these effects carry forward in time to affect the final crater geometry. The final effect is that, as melt flows back into the crater, it will solidify while in contact with the cooler side walls. This will effect the crater geometry and melt flow resulting from subsequent laser pulses, especially for deep holes.

4.2. Parameter Studies

Numerical simulations were performed for the parameters as listed in the Table II. The purpose of this multitude of runs is mainly to identify trends that link the laser parameters to material removal rates. Therefore, the in-depth study of a single drilled hole for temperature distribution, fluid configuration, and such is only secondary in the light of the primary objective. It is noteworthy to mention that the run times for these simulations are very high; for example, test case 1 typically takes about 12 h on a Sun Sparcstation 2. The table presents only what is gleaned out of a rather large number of runs which in the aggregate would have taken tens of hundreds of hours, not including the hours spent on debugging and aborted runs.

The velocity vector plot of the melt flow occurring at 600 μs for case (2) is shown in Fig. 9. The figure illustrates the radial movement of the melt flow driven by the radial pressure gradient. A typical laser intensity profile which is a function of space and time is shown in Fig. 10. The final geometric shapes of the craters drilled for the test cases 6 to 9b are shown in Fig. 11 through Fig. 16. The volume of the material removed was estimated by fitting the depth verses radius profile of the hole by a parabola and then integrating for the volume, giving

$$V \simeq \frac{\pi d_c a^2}{2}, \qquad [4.2.1]$$

where d_c is the depth of the hole at the center and a is the radius of the hole at the level of the original surface.

Calculations reveal the effects of different parameters, viz., the spatial and temporal characteristics of the incoming laser beam, the number of pulses, and the material properties. Qualitative trends could now be identified from these simulations. Table III compares the size of the craters drilled, energy deposited to the target, and the amount of material removed.

Calculated results indicate laser parameters had significant effects on the final crater geometry and qualitative trends could be identified. Cases 1, 2, and 5 and 6, 8a, and 9a comprise two sets of observations. The mesh density of the second set is twice that of the first; otherwise, these two sets have the same laser beam characteristics and material properties. It can be deduced that the material removal rate appears to be proportional to $I_0^{0.5}$, as opposed to the $I_0^{0.25}$-dependence predicted by some one-dimensional models. It can also be deduced that proportionality constant for the two sets of observations are different due to different mesh densities. Another comparison of the data indicates that the mass removed per joule absorbed appears

TABLE III

Quantitative Comparison of Numerical Results

No.	κ cm^2 s^{-1}	P_{max} W	E J	d_c μm	α μm	mg *rem*	mg/J
1	0.042	836	0.82	400	270	0.39	0.48
2	0.042	1672	1.65	520	280	0.55	0.33
2a	0.093	1672	1.65	960	280	0.99	0.60
3	0.042	3359	3.30	480	410	1.09	0.33
4	0.042	1672	2.67	930	270	0.88	0.33
5	0.042	3395	3.30	650	300	0.79	0.24
6	0.042	5067	4.95	520	280	0.54	0.11
7	0.042	5067	8.03	930	270	0.89	0.11
8a	0.042	2534	2.47	400	270	0.38	0.16
8b	0.042	2534	5.15	970	270	0.93	0.18
8a	0.042	2534	2.47	400	270	0.38	0.16
9a	0.042	10134	9.90	650	300	0.77	0.08
9b	0.042	10134	20.60	1410	300	1.67	0.08

to vary approximately as $I_0^{0.5}$. Relations such as these are very useful and should be investigated further.

The results show that the thermal properties of the target material, especially the thermal diffusivity, can significantly influence the LD process. A comparison of simulated craters for identical laser beam profiles is made for thermal diffusivities 0.042 cm^2/s and 0.093 cm^2/s (test cases 2 and 2a). The mass removed per joule absorbed nearly doubled when the thermal diffusivity was increased, resulting in a crater which was nearly twice deep. Another important thermal parameter is the heat of vaporization L_v, which affects the surface temperature and pressure and is kept constant in the simulations. For shallow craters, the pulse repetition rate was not found to be an important factor because the time needed for the melt to solidify was short, compared to the time between pulses. While numerical simulations have not been performed for deep holes (depth/diameter > 10), it is anticipated that for lower beam intensities with thick melt layers at the bottom of the hole, the repetition rate may be significant, particularly with regard to setting an upper limit on the rate. Some more qualitative observations can also be made from the simulations. For example, when the temporal peak was delayed (case 7), the taper became steep, because more energy was deposited and hence more material was removed. Also, after the second pulse (cases 8b and 9b), the lateral surface almost became vertical indicating a deep hole. It should be borne in mind that even though all the parameters are seemingly independent, for a given laser apparatus, it is sufficient, however, to specify the number of pulses, energy per pulse, and the spot size.

Experimental data obtained for five single pulse shots were found to be in agreement with respect to crater depth and diameter within roughly 25% with the corresponding numerical predictions. Considering the fact that the simulation of laser intensity profiles in time and space might have had 25% uncertainty in them, combined with a roughly 25% uncertainty in the energy deposited, the numerical results are trustworthy. Controlled experiments are planned for effective comparisons in the future. None of the experimental data are presented here, however.

This code can be used with any material as long as one knows the properties listed in Table I. In this simulation, material properties at elevated temperatures greater than the melting temperature were unknown for the material considered. Therefore, the surface tension was assumed to be constant and thermal conductivity and density were assumed to be the same in the solid and melt. The reflectivity was assumed to be zero because its modeling requires plasma/vapor interaction with the beam which was not carried out in the physical model. These are the limitations of the model and future work will eliminate some of them. However, the numerical model can be extended to 3D without much ado. The physical model can be enhanced to account for beam/plasma and beam/vapor interactions. There exists no comprehensive 2D model in the presently available literature for any reasonable comparison, however, good qualitative agreement was found with experimental observation.

5. CONCLUSION

A direct computer simulation of the laser drilling process in a turbine airfoil material was undertaken with many simplifying assumptions in the physical model. The numerical model assumes no variations of the pertinent variables in the azimuthal direction and hence a pseudo three dimensional analysis, viz., an axisymmetric problem (2D) was analyzed. The novel features in this method are threefolds. First, the laser melted pool surface is treated as a deformable free surface. Second, the impressed pressure and

temperature on the melt surface is provided by the gas dynamics model whose vaporization kinetics are discussed. Third, the resolidification of melt was modeled as well. The results of the simulations with many simplifications discussed are self-consistent among themselves and definite semi-quantitative trends could be established. Extensive experimental observations are not yet available, but the preliminary data compared favorably with the simulations, considering the uncertainties involved. The next logical step would be to relax the assumptions in the physical model one by one and conduct empirical testing and verification by experimental observations.

Improved treatment [16] of the gas dynamics of the metal vapor created during the LD process and possible 3D extension [17] of LD for oblique incidence will be reported elsewhere.

ACKNOWLEDGMENTS

The authors with profound regret share the demise of Professor W. W. Bowley who encouraged us all throughout this project. We thank Dr. Edward C. Wingfield of Fields Unlimited, Glastonbury, CT, Mr. Karl Schachtner and Mr. Jeff Hostetler of Pratt & Whitney Aircraft, CT., Mr. Ron Gagosz and Mr. Richard Frye of United Technologies Research Center, CT., for their funding, invaluable inputs, timely suggestions, and experimental data.

REFERENCES

1. J. Mazumder, *Opt. Eng.* **30**(8), 1208 (1991).
2. T. Zacharia, A. H. Eraslan, D. K. Aidun, and S. A. David, *Metall. Trans. B* 20 645 (1989).
3. C. Chan, J. Mazumder, and M. M. Chen, *Metall. Trans. A* **15,** 2175 (1984).
4. S. Kou and Y. H. Wang, *Metall. Trans. A* **17,** 2265 (1986).
5. S. Kou and D. K. Sun, *Metall. Trans. A* **16,** 203 (1985).
6. C. L. Chan and J. Mazumder, *J. Appl. Phys.* **62**(11), 4579 (1987).
7. M. Von Allmen, **47**(12), 5460 (1976).
8. A. Kar and J. Mazumder, *J. Appl. Phys.* **68**(8), 3884 (1990).
9. R. S. Patel and M. Q. Brewster, *J. Thermophys. Heat Transfer* **5**(1), 32 (1991).
10. B. D. Nichols, C. W. Hirt, and R. S. Hotchkiss, LA-8355, UC-32, and UC-34, August 1980 (unpublished).
11. L. D. Landau and E. M. Lifschitz, *Fluid Mechanics* (Pergamon, New York, 1959).
12. C. J. Knight, *AIAA J.* **17**(5), (1979).
13. R. A. Bellantone, Doctoral dissertation, University of Connecticut, 1992 (unpublished).
14. H. Callen, *Thermodynamics and an Introduction to Thermostatics,* (Wiley, New York, 1985).
15. R. Bellantone, R. K. Ganesh, Y. Hahn, and W. W. Bowley, in *10th International Invitational Symposium on the Unification of Numerical, Analytical & Experimental Methods, July 18–19, 1991* (WPI, Worcester, MA 01609).
16. R. Bellantone and Y. Hahn, *J. Appl. Phys.* **76**(3), (1994).
17. Y. Hahn, R. Bellantone, and R. K. Ganesh *J. Appl. Phys.,* submitted.